Structure and magnetic properties of Fe-Co alloy nanoparticles synthesized by pulsed-laser inert gas condensation

Structure and magnetic properties of Fe-Co alloy nanoparticles synthesized by pulsed-laser inert gas condensation

Nicola Patelli,[1] Francesco Cugini,[2] Di Wang,[3,4] Samuele Sanna,[1] Massimo Solzi,[2] Horst Hahn,[3] and Luca Pasquini[1]

1 - Department of Physics and Astronomy, University of Bologna, viale Berti-Pichat 6/2, 40127 Bologna, Italy

2 - Department of Mathematical, Physical and Computer Sciences, University of Parma, Parco Area delle Scienze 7/A, 43124 Parma, Italy

3 - Institute of Nanotechnology, Karlsruhe Institute of Technology, Hermann-von-Helmholtz-Platz 1, 76344 Eggenstein-Leopoldshafen, Germany

4- Karlsruhe Nano Micro Facility, Karlsruhe Institute of Technology, Hermann-von-Helmholtz-Platz 1, 76344 Eggenstein-Leopoldshafen, Germany

Abstract

Fe-Co alloy nanoparticles of different compositions (Fe content of 76, 51, and 30 at.%), along with pure Fe and Co nanoparticles, were prepared by pulsed-laser inert gas condensation, consisting in laser ablation of Fe-Co alloy targets under helium atmosphere. From the morphological point of view, the obtained nanoparticles have nearly spherical shape, follow a lognormal size distribution and exhibit little aggregation. X-ray diffraction and high-resolution electron microscopy coupled with electron energy loss spectroscopy show that the Fe-Co nanoparticles are single crystals with body-centred cubic structure. Furthermore, in the majority of nanoparticles the composition is highly uniform across the whole diameter and there is little variation in composition from one nanoparticle to another. Exposure to non-inert atmosphere leads to the formation of a core@shell metal@oxide morphology characterized by a spinel oxide shell of 2-3 nm around the metallic alloy core. All samples display a ferromagnetic behaviour, characterized by a hysteretic magnetization loop. The saturation magnetization attains a maximum value of 2.43 Bohr magnetons per atom for Fe content of 76 at.%, in agreement with the Slater-Pauling curve for alloys of 3d elements. Instead, the coercive field, ranging from 29 to 60 kAm^{-1}, is much larger than the reported values for polycrystalline bulk Fe-Co compounds and monotonically increases from pure Fe to pure Co. These results demonstrate that pulsed-laser inert gas condensation allows to prepare high-quality nanoalloys with tailorable magnetic properties, overcoming the limitations of thermal evaporation methods with respect to compositional control.

Keywords: Nanostructured Materials; Metals and Alloys; Magnetically Ordered Materials; Pulsed Laser Ablation; Transmission Electron Microscopy; Magnetisation

Introduction

Since the early advent of metallurgy, mixing different elements into alloys and intermetallic compounds allowed mankind to extend the properties of metallic systems. The fine control over composition and structure promoted the tailoring of materials with well-defined mechanical, magnetic, optical, electronic and catalytic properties that are crucial to many applications.

It is no surprise that, in the contemporary days of nanoscience, the centre stage has been taken by the ambition to achieve a similar control over the composition and structure of nanomaterials. In this context, the term *nanoalloys* was coined to indicate nanoscale objects, such as clusters, nanoparticles (NPs), and nanowires, constituted by two or more elements [1,2].

Nanoalloys can be fabricated by different techniques, which include vapour condensation, chemical reduction, thermal decomposition of transition-metal complexes, electrochemical synthesis, and even biosynthesis [1]. Vapour condensation is a physical method that relies on the production of atomic vapours followed by their condensation in a cooling atmosphere, usually an inert gas able to induce supersaturation and homogeneous nucleation [3]. Compared to most wet chemistry techniques, it offers the advantage of providing ligand-free, self-standing, high purity nanoalloys with the drawback of requiring more costly equipment. Different options are available for vapour generation starting from solid precursors, such as thermal evaporation, laser ablation, ion or magnetron sputtering, and electrical discharge. Whatever the vaporization method of choice, the stoichiometry of the sample must be precisely controlled and uniform throughout. This is seldom achieved by thermal evaporation of precursor alloys, because the evaporation rates of the constituting elements are usually different and strongly temperature dependent [4]. To bypass this limitation, rate-controlled evaporation of elemental precursors from different sources may be employed [5], although it does not guarantee full vapour mixing prior to condensation. An alternative approach employs magnetron sputtering of alloy targets at higher pressure than conventionally used for thin-film deposition; in this setup, the condensed nanoparticles are usually carried away by gas expansion through a nozzle [6].

Pulsed-laser ablation in high vacuum is a technique usually adopted for deposition of thin films with complex stoichiometry. In the last two decades, pulsed-laser ablation in liquid emerged as a flexible method for the synthesis of colloidal NPs with various compositions, including nanoalloys of metastable elements and metal oxides [7,8]. Besides ablating a bulk target immersed in a liquid, various liquids can be used as a direct target, including solutions of colloidal particles. In fact, under laser irradiation, particles in the suspension can be transformed into particles with different size and same or different shape, crystal phase, and stoichiometry. The synthesis and processing of colloids by laser irradiation has emerged as a powerful tool for synthesizing ligand-free nanomaterials in a liquid [9].

In a yet different approach, pulsed-laser ablation can be combined with inert gas condensation (PL-IGC) to overcome the problem of stoichiometric control typical of thermal vapour sources, thus gaining access to the preparation of a broad range of nanoalloys, which are not dispersed in a liquid. The application of this versatile method to elements, oxides and alloys has been demonstrated recently by Bag et al [10]. The present work reports on the structure and magnetic properties of Fe-Co alloy NPs prepared by PL-IGC with Fe contents of 76, 51, and 30 wt%, along with pure Fe and Co NPs. Fe-Co nanoalloys are of great interest thanks to their excellent magnetic properties [11,12] that make them prospective candidates for many applications such as: cell separation and drug delivery [13,14], hyperthermia [15,16], contrast enhancement in magnetic resonance imaging [17], high-frequency power applications [18], electromagnetic wave absorption [19,20]. Moreover, Fe-Co NPs show interesting catalytic properties for CO_2 hydrogenation, reaching better performances than the pure metallic elements [21,22]. Therefore, the development of novel methods for the preparation of Fe-Co NPs with tailorable magnetic properties, high purity and negligible aggregation is highly desirable.

This work demonstrates that by using PL-IGC, one readily obtains Fe-Co nanoalloys, the composition of which replicates very well the one of the target precursor. Moreover, in the vast majority of NPs, the distribution of Fe and Co is highly uniform throughout the volume. In terms of morphology and structure, the nanoalloys appear as nearly spherical single-crystals with body-centred cubic structure, in agreement with the Fe-Co phase diagram. Interestingly, their magnetic properties display a high saturation magnetization that follows the dependence on composition predicted by the Slater-Pauling curve for alloys of 3d elements. These results showcase the possibility of achieving both a high purity and a fine control over the stoichiometry and properties of binary NPs by means of the PL-IGC technique.

Materials and Methods

Nanoparticles synthesis by PL-IGC

Fe-Co alloy NPs were synthesized by a combination of Pulsed Laser ablation and Inert Gas Condensation (PL-IGC) in a helium atmosphere. Fe-Co targets (*EvoChem GmbH,* 99.95% purity) with different Fe contents (30, $51, 76$ at.$\%$) were used as precursors to obtain nanoalloys of different composition.
The targets were ablated by scanning the surface with an infrared pulsed laser (Yb:YAG, $\lambda = 1030$ nm), having a pulse duration < 10 ps and a repetition rate of 800 kHz. The laser was focused on the target by using an f-theta lens with a focal length of 254 mm. Preliminary experiments were carried out under different conditions using an elemental Fe target (SurfaceNet GmbH, 99.95% purity) in order to determine the laser power (20 W) and He pressure (1.0 kPa) that optimize the NPs yield. For the synthesis of all Fe-Co nanoalloys, the selected laser power was 20 W and the diameter of the focused spot was 25 μm, corresponding to an irradiance of 4.1×10^{10} W cm^{-2}. Full details of the experimental setup are reported in the Supplementary Material (SM) and in a previous publication [10].

The NPs condensed within the laser plume were rapidly removed from the laser-irradiated zone by the incoming He flow, which transported the NPs towards a collection surface consisting of a stainless steel spiral internally cooled by liquid nitrogen. As shown in Figure S1, the collection unit can be sealed by means of two gate valves. In this way, it was possible to seal the collection unit under a slight Ar overpressure and open it inside a glove box, in order to scrape off the NPs for subsequent structural analyses.

Structural and morphological characterization

The morphology, size distribution and composition of the NPs were analysed using a Zeiss LEO 1530 field emission scanning electron microscope (FE-SEM) equipped with *in-lens* electron detector and energy-dispersive x-ray microanalysis (EDX).

The crystalline structure of Fe–Co alloy NPs was determined by x-ray diffraction (XRD) with a Bragg-Brentano Bruker diffractometer employing a liquid Ga jet as anode ($\lambda_{K\beta} = 1.20759$ Å). The NPs were loaded inside the Ar-filled glovebox on an XRD stage, which was sealed by a kapton window to prevent air exposure.

The structure and composition at the single NP level was investigated by a *FEI Titan 80-300* transmission electron microscope (TEM) operated at 300 kV and equipped with a spherical aberration corrector and a *Gatan Tridiem 965* image filter for energy-filtered TEM (EFTEM) imaging. Line profiles of atomic composition were measured by collecting electron energy loss spectra (EELS) in scanning TEM (STEM) mode along with high-angle annular dark field (HAADF) intensities by scanning the electron beam across the particle. The TEM specimens were prepared inside the glove box by dispersing the NPs onto gold grids coated with a holey carbon film and loaded onto a Gatan vacuum transfer holder without air exposure.

Magnetic measurements

The magnetic properties of NPs were investigated with an extraction magnetometer (MAGLAB SYSTEM2000 by Oxford Instruments). Magnetic hysteresis loops were collected at room-temperature (T = 295 ± 1 K) with a maximum applied magnetic field of 1.8 T. The NPs were sealed in quartz vials filled with a low-pressure He atmosphere, to avoid oxidation. A Teflon cap was used to fix the powder and prevent the movement of NPs during the measurement.

Results and Discussion

Dependence of nanoparticles size and yield on synthesis conditions

Two preliminary sets of experiments, using an elemental Fe target, were carried out to evaluate the influence of a) laser power and b) He gas pressure on the yield rate and size distribution of NPs. Figure 1 reports the FE-SEM images and corresponding size distributions of Fe NPs synthesized at laser powers of 10, 20, and 30 W under the same He pressure of 1.0 kPa.

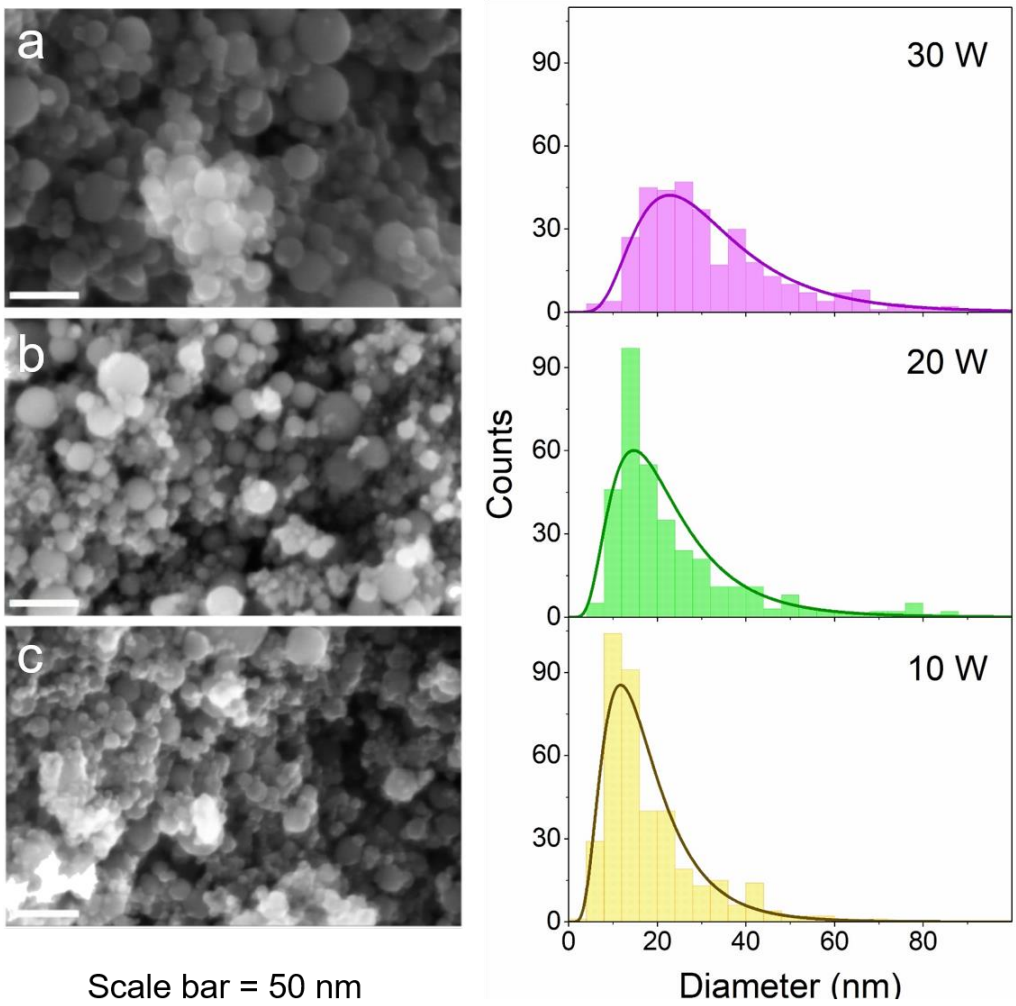

Figure 1. In-lens FE-SEM images of elemental Fe NPs synthesized by PL-IGC at p(He)=1.0 kPa using different laser powers of 30W (a), 20 W (b), and 10W (c). The horizontal scale bar is 100 nm. The corresponding distributions of NPs diameters obtained from analysis of each FE-SEM image are shown to the right; the parameters of the fitted lognormal functions are reported in Table S1.

The NPs exhibit an almost spherical shape and their diameter d follows a lognormal distribution [23], i.e. $\ln d$ is Gaussian around a median value $\ln \tilde{d}$ with standard deviation $\ln \sigma$:

$$f_{LN}(\ln d) = \frac{1}{(2\pi)^{1/2} \ln \sigma} \exp\left(-\frac{(\ln d - \ln \tilde{d})^2}{2(\ln \sigma)^2}\right) \quad (1)$$

It is clear that both the average diameter and the width of the distribution shift towards larger values with increasing power, the effect being particularly evident at 30 W. The parameters of the lognormal distribution that best fits the experimental data are reported in Table S1 of the SM. The NPs yield, determined by weighting the NPs collected after the synthesis, was about 200 mg/hour at 20 W but decreased by almost two orders of magnitude at 10 W.

The influence of He pressure on NPs size was less evident: Figure S3 of the SM shows FE-SEM images and size distributions of Fe NPs synthesized at the same 20 W power under 0.5, 1.0, and 2.0 kPa He pressure (the distribution parameters are listed in Table S2). At the lowest He pressure, the NPs tend to stick to the inner walls, partially coating the viewport window that allows the laser to access the chamber, resulting in a loss of power and potential hazardous heating of the window itself. This issue negatively impacts the NPs production rate causing a drastic decrease of the yield at 0.5 kPa. For these reasons, the subsequent synthesis of Fe-Co alloy NPs was conducted at 20 W power under a He pressure of 1.0 kPa.

Structure, composition and size distribution of the NPs ensemble

The average composition of $Fe_{100-x}Co_x$ nanoalloys determined by SEM-EDX shows an excellent agreement with that of the precursor target, as reported in Table 1, demonstrating that the PL-IGC method is very effective in preserving the original stoichiometry.

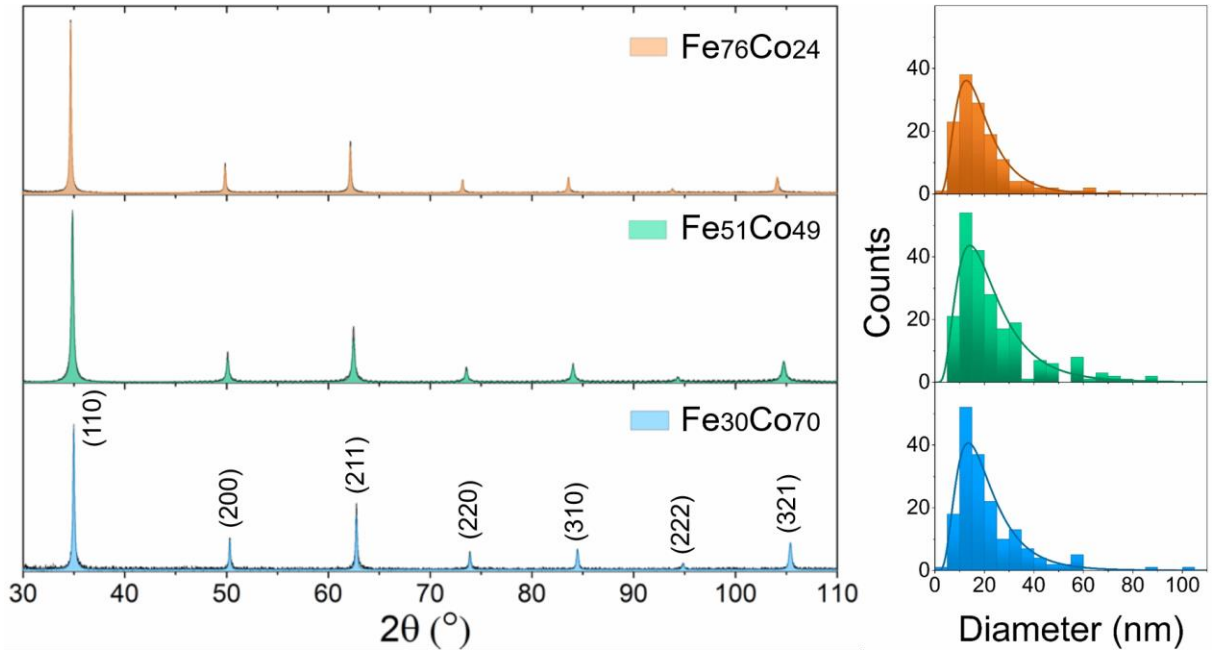

Figure 2. XRD patterns ($\lambda = 1.20759$ Å) of $Fe_{100-x}Co_x$ NPs prepared by PL-IGC at 20 W laser power and 1.0 kPa He pressure. The black solid lines are the experimental data, while the coloured areas represent the calculated contribution from a *bcc* solid solution. The Miller indices of the Bragg reflections are indicated. The corresponding distribution of NPs diameters, obtained from the analysis of EFTEM zero-loss images, are shown to the right. The lattice parameter and the parameters of the distributions are reported in Table 1.

The XRD patterns displayed in Figure 2, which also lists the Miller indices assigned to the observed Bragg reflections, reveal the presence of a single *bcc* phase for all compositions. This finding is in agreement with the Fe-Co phase diagram, which predicts a homogeneous Fe-Co solid solution up to about 80 at.% Co [24]. The lattice parameter of the *bcc* phase decreases with increasing Co content (see Table 1), as highlighted by the shift of the Bragg reflections toward higher angles that becomes particularly evident for high Miller indices, e.g. the (321) reflection in Figure 2. This change of lattice parameter is expected on account of the smaller atomic radius of Co compared to Fe. Superlattice reflections suggestive of a B2-type ordered phase are not detected, even if long-range order is predicted below a composition-dependent critical temperature (about 730 °C for an equiatomic alloy). This is due to the fact that B2 ordering requires prolonged annealing at elevated temperatures [24] and is therefore unlikely to develop during the fast cooling of the laser plume. Bragg reflections of oxide phases are not visible in the XRD patterns, suggesting that by proper handling of the nanoalloys it is possible to keep oxidation to a minimum. This high purity allows to attain a high saturation magnetization, as described later on. In summary, the picture provided by XRD is that of a disordered (A2-type) *bcc* Fe-Co alloy for all compositions.

Table 1. Fe content (defined as Fe/(Fe+Co) in at.%) in the target precursor and in the Fe-Co NPs determined by SEM-EDS, lattice parameter a of the *bcc* phase, average NPs diameter $\langle d \rangle$, median $\tilde{d}$ and width parameter $\ln \sigma$ of the lognormal distribution (see equation (1)) for the three $Fe_{100-x}Co_x$ NPs. The numbers within parenthesis represent the standard error in units of the last significant digit.

Sample name	Fe% precursor (at.%)	Fe% in NPs (at.%)	a (Å)	$\langle d \rangle$ (nm)	$\tilde{d}$ (nm)	$\ln \sigma$
$Fe_{76}Co_{24}$	75.8(5)	75.6(5)	2.8661(2)	21.1	18.2	0.55
$Fe_{51}Co_{49}$	50.6(5)	50.7(5)	2.8535(2)	23.4	19.8	0.58
$Fe_{30}Co_{70}$	29.8(5)	29.5(5)	2.8406(2)	19.1	16.7	0.52

The NPs size distributions are displayed in Figure 2, while the corresponding parameters are reported in Table 1. We notice that both the average diameter and the width of the distribution exhibit a small variation among the three samples and do not show a correlation with the composition. This feature may be related to the similar heat of vaporization of Co and Fe (≈ 375 and 350 kJ/mol, respectively) [25] and to the homogeneous alloy nature of the precursor target. These data suggest that Fe and Co behave likewise within the plasma plume generated by laser interaction with the metal target and that condensation and coagulation of the two elements occurs equally [26]. The presence of larger NPs in the distribution tail has already been reported for other classes of materials obtained via PL-IGC [10].

Composition and crystalline structure of individual NPs

Figure 3 shows EFTEM images recorded on the $Fe_{30}Co_{70}$ NPs. The Fe, Co, and O elemental maps are displayed in the subpanels to the right, while the main panel shows the bright-field zero-loss image that conveys morphological information. Noteworthy, Fe and Co maps are very similar, demonstrating that Fe and Co are homogeneously distributed down to the single NP level. This finding is consistent with the presence of a single phase in the XRD patterns and confirms that PL-IGC gives rise to a vast majority of alloy NPs with uniform composition. Nevertheless, brighter spots visible only in one map suggest that a minority of particles deviate from the average composition. From the inspection of several EFTEM maps, we estimate that such NPs amount to about 10% of the total. The oxygen elemental map, despite featuring a higher noise because of the smaller signal level, highlights that oxygen is more abundant in the near-surface regions of the NPs. The same semi-quantitative information is obtained for the other two compositions.

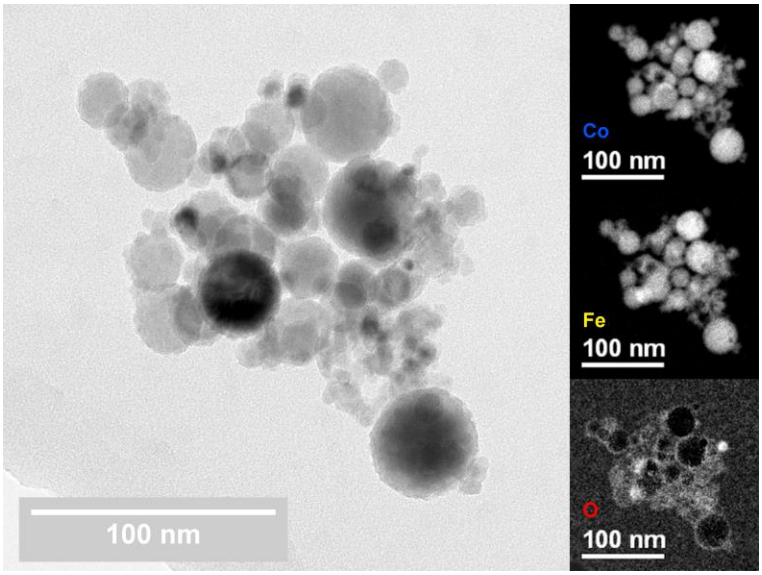

Figure 3. Main panel: EFTEM zero-loss image representative of $Fe_{30}Co_{70}$ NPs. The corresponding Fe, Co, and O elemental maps are reported in the panels to the right.

A quantitative and spatially resolved analysis of elemental distribution within single NPs is provided by the STEM-EELS profiles presented in Figure 4 for all compositions. The Fe, Co, and O atomic percentages reported in the insets were obtained from the analysis of EELS acquired along the red arrows in the HAADF images. In agreement with the results of EFTEM imaging, it is possible to identify two different composition regions within a single NP: an oxygen-rich shell and a metallic core. The remarkable feature of PL-IGC NPs is that the Fe/Co ratio remains constant along the core region, showing that the average composition determined by SEM-EDX corresponds to the local composition within the NPs.

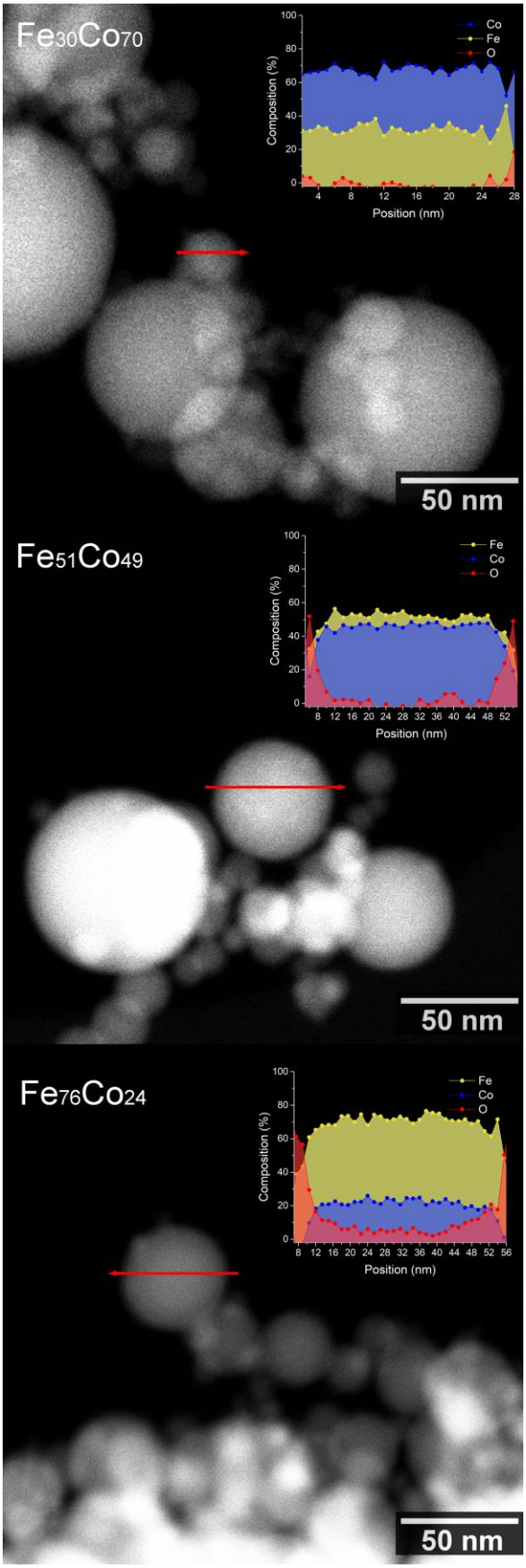

Figure 4. STEM image of NPs with Fe content of 30, 51, and 76 at.% increasing from top to bottom. The top-right inset in each subpanel reports a line scan of the atomic percentages inside a NP, obtained from the quantitative analysis of EELS recorded along the red arrows. In particular, the yellow, blue, and red lines represent the atomic percentages of Fe, Co, and O, respectively.

The presence of a metal@oxide core@shell structure is confirmed by the high-resolution TEM (HRTEM) micrograph shown in Figure 5 for sample $Fe_{76}Co_{24}$. In all observed NPs, the core appears as a single crystal; the lattice spacing of 2.02 Å visible in the core of Figure 5 corresponds to the (110) interplanar spacing of a *bcc* structure with lattice parameter of 2.86 Å, in agreement with the results of XRD reported in Table 1. The shell exhibits the interplanar spacing of 2.53 Å characteristic of a spinel oxide $Fe_{3-x}Co_xO_4$. The thickness of the shell is $\delta \approx 2 - 3$ nm, which is a typical value observed in this kind of NPs [27].

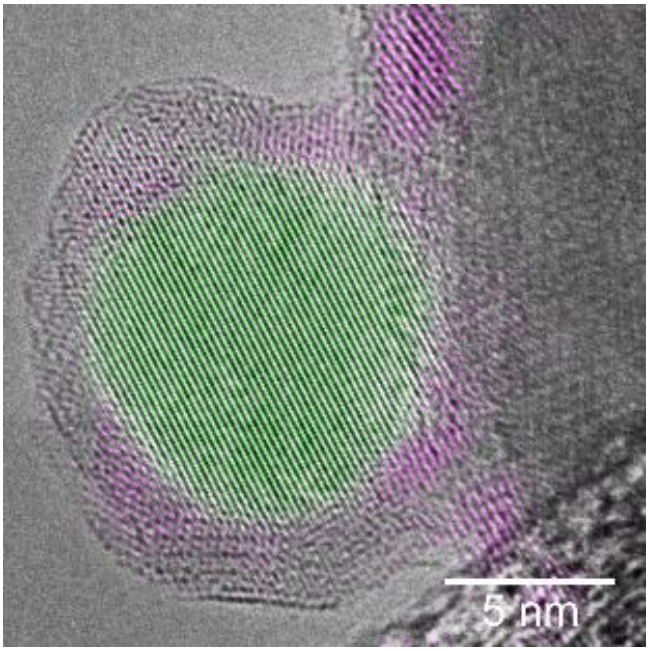

Figure 5. HRTEM image for the $Fe_{76}Co_{24}$ nanoalloy: the areas characterized by the (110) lattice planes of a *bcc* Fe-Co alloy, having an interplanar spacing of 2.02 Å, are coloured in green, while the areas that highlight the (~~331~~311) lattice planes of a spinel oxide $Fe_{3-x}Co_xO_4$ with interplanar spacing of 2.53 Å, are coloured in magenta.

The results of magnetic measurements described in the next section prove that the oxide content of the as-synthesized NPs is very small, i.e. much below the volumetric oxide/metal ratio of $6\delta/d$ that can be estimated for a core@shell NP. Moreover, also XRD does not show evidence of oxide formation. We therefore conclude that the thin oxide shell detected by TEM observations forms because of residual oxygen either during the transfer procedure or within the TEM column. Nevertheless, this metal@oxide morphology is relevant because it develops quickly when the NPs are exposed to a non-perfectly inert atmosphere. Furthermore it is usually observed that the oxide shell is effective in protecting the NPs against further oxidation [28].

Magnetic properties

The room-temperature ($T = 295 \pm 1$ K) magnetic hysteresis loops of $Fe_{100-x}Co_x$ NPs (x=24, 49, 70) and pure elements (Fe, Co) NPs are reported in Figure 6. All the samples show a ferromagnetic behaviour, characterized by a hysteretic $M(H)$ loop. This result agrees with the distribution of NPs diameters (Table 1): the average dimension of NPs is larger than the critical superparamagnetic (SPM) size at room temperature (the SPM blocking diameter at 300 K is 16 nm for Fe, 8 nm for Co in the hexagonal-closed-packed (*hcp*) crystal structure and about 12 nm for the face-centred cubic (*fcc*) Co phase) [29,30]. The larger, non-SPM, particles determine the hysteretic character of the loop. Instead, the NPs with a diameter below the SPM critical diameter contribute to the stretching of the loop. The magnetization, almost saturated at $\mu_0 H = 1$ T, strongly depends on the composition (Figure 7, Table 2). The maximum magnetization ($\sigma_s = 239.6$ A m^2 kg^{-1}, corresponding to a

magnetic moment per atom $\mu = 2.43$ Bohr magnetons (μ_B)), obtained for the $Fe_{76}Co_{24}$ alloy, approaches the largest room-temperature magnetization of any bulk material (240 Am^2kg^{-1}, 2.46 μ_B per atom), measured in a $Fe_{65}Co_{35}$ alloy [29,31,32]. The variation of the Fe/Co ratio from the $Fe_{76}Co_{24}$ composition leads to the decrease of saturation magnetization, following the Slater-Pauling curve for binary alloys of 3d elements (Figure 7) [29,33]. The measured moments of pure Fe and Co NPs (2.18 ± 0.02 μ_B and 1.74 ± 0.01 μ_B) agree with the values reported for the corresponding bulk materials [29]. For the Co sample, the obtained value of the magnetic moment suggests that many of the Co NPs are in the *fcc* crystal structure, which can be stabilized in nanoscale magnetic structures and is characterized by a higher moment with respect to the *hcp* phase [29,34,35]. The very large values of saturation magnetization of all prepared alloys, in agreement with those of bulk materials [31], demonstrate the non-oxidation and the good crystallization of PL-IGC NPs without the need of post-synthesis annealing treatments, which are required for other preparation methods [36–39].

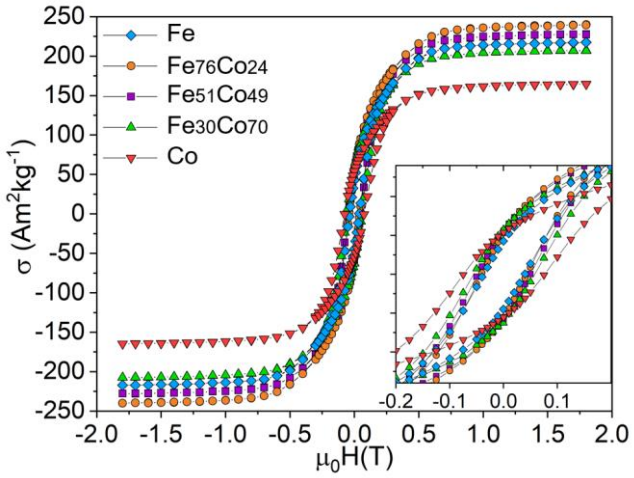

Figure 6. Magnetic hysteresis loops collected at $T = 295$ K for the $Fe_{100-x}Co_x$ alloys NPs (x=24, 49, 70) and for the pure elements (Fe, Co) NPs. Inset: enlargement of the hysteresis loops at low field.

Table 2. Valence electrons per atom, saturation magnetization (σ_s), magnetic moment per atom (μ), coercivity (H_c) and reduced remanence (m_r = magnetic remanence/ saturation magnetization) of $Fe_{100-x}Co_x$ NPs.

	Valence e- /atom	σ_s (Am^2kg^{-1})	**μ/atom** (μ_B)	H_c (kA m^{-1})	m_r
Fe	8	217.4 ± 1.9	2.17 ± 0.02	29 ± 1.6	0.20
$Fe_{76}Co_{24}$	8.24	239.6 ± 2.5	2.43 ± 0.02	33 ± 1.6	0.22
$Fe_{51}Co_{49}$	8.49	227.7 ± 2.2	2.34 ± 0.02	37 ± 1.6	0.25
$Fe_{30}Co_{70}$	8.71	207 ± 1.7	2.16 ± 0.02	45 ± 1.6	0.28
Co	9	164.5 ± 1.3	1.74 ± 0.01	60 ± 1.6	0.33

Unlike the saturation magnetization, the coercivity shows a monotonous variation with the composition, increasing from 29 ± 3 kA m^{-1} of Fe NPs to 60 ± 3 kA m^{-1} of Co sample (Figure 8, Table 2]. This trend, observed also for $Fe_{100-x}Co_x$ (x = 0 – 60) bulk alloys prepared by mechanical alloying [32], can be explained considering the increase of magnetocrystalline anisotropy K from Fe ($K = 48$ kJ m^{-3} [29]) to Co ($K \approx 110$ kJ m^{-3} for the *fcc* phase [30,40] and $K = 410$ kJ m^{-3} for the *hcp* phase [29]). By considering the coherent magnetization reversal of an array of non-interacting spherical particles with a random distribution of anisotropy axes in the framework of the Stoner-Wohlfarth model, we can estimate the expected coercivity for Fe and Co

ferromagnetic single-domain NPs as $H_c \approx K/\mu_0\sigma_s$ [29,34]. This expected coercivity turns out to be 23 kA m^{-1} for Fe and about 60 kA m^{-1} for Co. The approximation of the cubic anisotropy of *bcc* Fe and *fcc* Co to uniaxial anisotropy can be acceptable considering that, in real materials, structural defects and surface deformations lead to a dominant uniaxial anisotropy [34].

The difference between the calculated coercivity of Fe NPs and the experimental ones, can be due to the contribution of a shape anisotropy $K_s \approx (1-3N)\sigma_s/2$, where N is the demagnetizing factor [29,41]. Considering the large magnetization of Fe-Co alloys, a small deviation from the spherical symmetry of NPs can induce a large contribution to anisotropy. For example, in the case of Fe NPs, a 1% change of the ratio between the ellipsoid axes results in a contribution to the coercivity of about 3 kA m^{-1}. Indeed, the presence of non-perfectly spherical NPs can be evinced from the TEM image in Figure 3. In the case of Co NPs, the effect of shape anisotropy is less important considering the larger value of magnetocrystalline anisotropy, the probable presence of *hcp*-Co particles with a large coercivity [34] and the larger critical single domain size (30 nm for *fcc* Co [42], 112 nm for *hcp* Co and 20 nm for Fe [29]). Indeed, the coercivity is reduced moving towards a non-coherent magnetization reversal mechanism, which occurs for larger NPs (the maximum particle diameter for coherent rotation is 24 nm for Fe and 17 nm for *hcp* Co [29]).

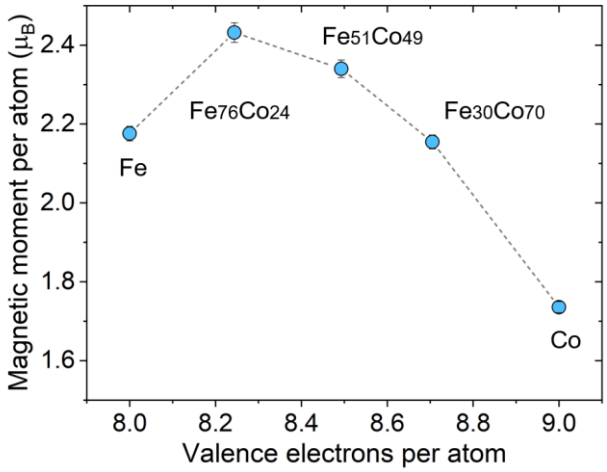

Figure 7. Magnetic moment per atom of $Fe_{100-x}Co_x$ NPs as a function of the valence electrons per atom.

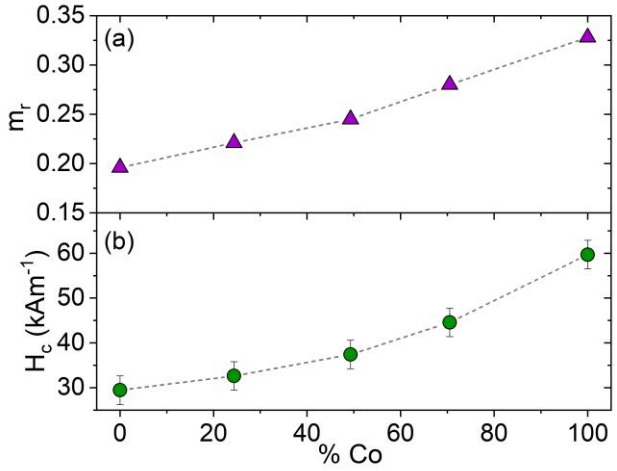

Figure 8. (a) Reduced remanence m_r and (b) coercivity H_c of $Fe_{100-x}Co_x$ NPs as a function of Co % content.

Moreover, the combination of the increase of critical single-domain size and coherent-rotation size and the decrease of SPM blocking size with Co content, justifies the increase with Co of the reduced remanence, calculated as the ratio between the magnetic remanence and the saturation magnetization (Figure 8, Table 2) [29]. Indeed, in the case of Fe NPs, many particles have a size below the SPM critical size (16 nm) or above the single-domain critical size (20 nm) and the critical coherent-rotation size (24 nm). [29] For these particles the coercivity is reduced, or totally cancelled in the case of SPM, thus resulting in a decrease of both hysteresis width and remanence. For the Co sample, whose particles are mainly ferromagnetic and single-domain [42], this effect is weaker, and the remanence increases.

Finally, the hysteresis loop was measured also for a sample of $Fe_{30}Co_{70}$ exposed to air for 72h (Figure 9). The oxidation of the NPs results in a 31% reduction of saturation magnetization and in the decrease of coercivity. The decrease of magnetization can be explained considering a shell of 2-3 nm of $Fe_{3-x}Co_xO_4$ oxide ($\sigma_S = 86 - 92$ A $m^2 kg^{-1}$ [29]), as observed by HRTEM images. Whereas, the reduction of coercivity results from the decrease of the Fe-Co crystallite size due to oxidation.

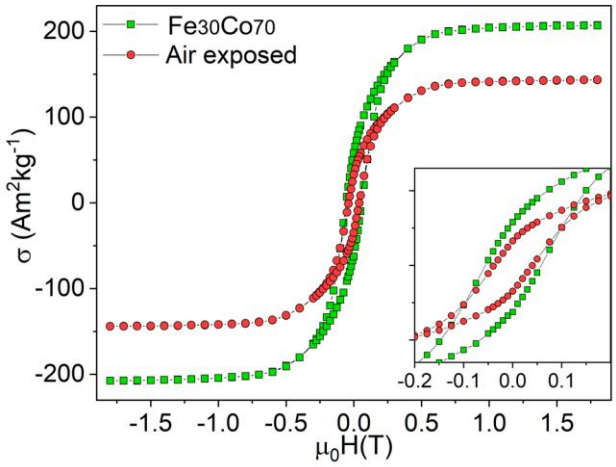

Figure 9. Magnetic hysteresis loop of a $Fe_{30}Co_{70}$ NPs sample exposed to air for 72 h (red circles) in comparison with the loop of non-oxidized sample (green square).

Conclusions

This work demonstrates the use of PL-IGC to prepare magnetic NPs that exhibit a number of appealing features: nearly spherical shape, little aggregation, high purity, and single crystal nature. The most remarkable aspect is the precise control over composition, which replicates very well the one of the ablated target precursor and displays good homogeneity among different NPs. Furthermore, the elemental distribution is uniform across the entire volume for the majority of NPs investigated by TEM. These features mark the superior characteristics of pulsed-laser ablation compared to thermal evaporation in the inert gas condensation of nanoalloys. The clear composition dependence of magnetic properties such as the saturation magnetization, which peaks at 2.43 Bohr magnetons for the Fe-rich alloy in full agreement with the Slater-Pauling curve for alloys of 3d transition metals, highlights the strong potential of PL-IGC in the precise tailoring of nanomaterials properties. As a consequence, the obtained alloy NPs can be considered an interesting model system that allows the fine tuning of the extrinsic magnetic properties, such as coercivity and remanence, from pure Fe

through the nanoalloys to pure Co, exploiting the regular variation of intrinsic magnetic properties and magnetization reversal mechanism.

Acknowledgements

DW and HH acknowledge the use of electron microscopy facilities of the Karlsruhe Nano Micro Facility. HH thanks the Deutsche Forschungsgemeinschaft for financial support under HA 1344/38-1. FC and MS thank D. Pontiroli (University of Parma) for his assistance in samples preparation for magnetic measurements.

References

[1] R. Ferrando, J. Jellinek, R.L. Johnston, Nanoalloys: From Theory to Applications of Alloy Clusters and Nanoparticles, Chem. Rev. 108 (2008) 845–910. doi:10.1021/cr040090g.

[2] F. Calvo, Thermodynamics of nanoalloys, Phys. Chem. Chem. Phys. 17 (2015) 27922–27939. doi:10.1039/C5CP00274E.

[3] M. Malekzadeh, M.T. Swihart, Vapor-phase production of nanomaterials, Chem. Soc. Rev. (2021). doi:10.1039/d0cs01212b.

[4] G. Rossi, M. Calizzi, V. Di Cintio, S. Magkos, L. Amidani, L. Pasquini, F. Boscherini, Local Structure of V Dopants in TiO_2 Nanoparticles: X-ray Absorption Spectroscopy, Including Ab-Initio and Full Potential Simulations, J. Phys. Chem. C. 120 (2016) 7457–7466. doi:10.1021/acs.jpcc.5b12045.

[5] N. Patelli, A. Migliori, V. Morandi, L. Pasquini, Interfaces within biphasic nanoparticles give a boost to magnesium-based hydrogen storage, Nano Energy. 72 (2020) 104654. doi:10.1016/j.nanoen.2020.104654.

[6] P. Grammatikopoulos, S. Steinhauer, J. Vernieres, V. Singh, M. Sowwan, Nanoparticle design by gas-phase synthesis, Adv. Phys. X. 6149 (2016) 1–20. doi:10.1080/23746149.2016.1142829.

[7] H. Zeng, X.W. Du, S.C. Singh, S.A. Kulinich, S. Yang, J. He, W. Cai, Nanomaterials via laser ablation/irradiation in liquid: A review, Adv. Funct. Mater. 22 (2012) 1333–1353. doi:10.1002/adfm.201102295.

[8] Vincenzo Amendola, Moreno Meneghetti, What controls the composition and the structure of nanomaterials generated by laser ablation in liquid solution?, Phys. Chem. Chem. Phys. 15 (2013) 3027–3046. doi:10.1039/C2CP42895D.

[9] D. Zhang, B. Gökce, S. Barcikowski, Laser Synthesis and Processing of Colloids: Fundamentals and Applications, Chem. Rev. 117 (2017) 3990–4103. doi:10.1021/ACS.CHEMREV.6B00468.

[10] S. Bag, A. Baksi, D. Wang, R. Kruk, C. Benel, M.R. Chellali, H. Hahn, Combination of pulsed laser ablation and inert gas condensation for the synthesis of nanostructured nanocrystalline, amorphous and composite materials, Nanoscale Adv. 1 (2019) 4513–4521. doi:10.1039/c9na00533a.

[11] T. Hasegawa, S. Kanatani, M. Kazaana, K. Takahashi, K. Kumagai, M. Hirao, S. Ishio, Conversion of FeCo from soft to hard magnetic material by lattice engineering and nanopatterning, Sci. Rep. 7 (2017). doi:10.1038/s41598-017-13602-x.

[12] G. Ennas, A. Falqui, S. Marras, C. Sangregorio, G. Marongiu, Influence of Metal Content on Size, Dispersion, and Magnetic Properties of Iron−Cobalt Alloy Nanoparticles Embedded in Silica Matrix, Chem. Mater. 16 (2004) 5659–5663. doi:10.1021/CM048761E.

[13] G. Reiss, A. Hütten, Magnetic nanoparticles: Applications beyond data storage, Nat. Mater. 4 (2005)

725–726. doi:10.1038/nmat1494.

[14] A. Hütten, D. Sudfeld, I. Ennen, G. Reiss, W. Hachmann, U. Heinzmann, K. Wojczykowski, P. Jutzi, W. Saikaly, G. Thomas, New magnetic nanoparticles for biotechnology, J. Biotechnol. 112 (2004) 47–63. doi:10.1016/j.jbiotec.2004.04.019.

[15] C.S.S.R. Kumar, F. Mohammad, Magnetic nanomaterials for hyperthermia-based therapy and controlled drug delivery, Adv. Drug Deliv. Rev. 63 (2011) 789–808. doi:10.1016/j.addr.2011.03.008.

[16] B. Mehdaoui, J. Carrey, M. Stadler, A. Cornejo, C. Nayral, F. Delpech, B. Chaudret, M. Respaud, Influence of a transverse static magnetic field on the magnetic hyperthermia properties and high-frequency hysteresis loops of ferromagnetic FeCo nanoparticles, Appl. Phys. Lett. 100 (2012). doi:10.1063/1.3681361.

[17] W.S. Seo, J.H. Lee, X. Sun, Y. Suzuki, D. Mann, Z. Liu, M. Terashima, P.C. Yang, M. V. McConnell, D.G. Nishimura, H. Dai, FeCo/graphitic-shell nanocrystals as advanced magnetic-resonance-imaging and near-infrared agents, Nat. Mater. 5 (2006) 971–976. doi:10.1038/nmat1775.

[18] Y.J. Tang, F.T. Parker, H. Harper, A.E. Berkowitz, Q. Jiang, D.J. Smith, M. Brand, F. Wang, Co50Fe50 fine particles for power frequency applications, IEEE Trans. Magn. 40 (2004) 2002–2004. doi:10.1109/TMAG.2004.832505.

[19] R. Lv, F. Kang, J. Gu, X. Gui, J. Wei, K. Wang, D. Wu, Carbon nanotubes filled with ferromagnetic alloy nanowires: Lightweight and wide-band microwave absorber, Appl. Phys. Lett. 93 (2008) 2006–2009. doi:10.1063/1.3042099.

[20] Y. Zhang, P. Wang, Y. Wang, L. Qiao, T. Wang, F. Li, Synthesis and excellent electromagnetic wave absorption properties of parallel aligned FeCo@C core-shell nanoflake composites, J. Mater. Chem. C. 3 (2015) 10813–10818. doi:10.1039/c5tc02146d.

[21] R. Satthawong, N. Koizumi, C. Song, P. Prasassarakich, Bimetallic Fe–Co catalysts for CO2 hydrogenation to higher hydrocarbons, J. CO2 Util. 3–4 (2013) 102–106. doi:10.1016/J.JCOU.2013.10.002.

[22] M. Calizzi, R. Mutschler, N. Patelli, A. Migliori, K. Zhao, L. Pasquini, A. Züttel, CO 2 Hydrogenation over Unsupported Fe-Co Nanoalloy Catalysts, Nanomater. 2020, Vol. 10, Page 1360. 10 (2020) 1360. doi:10.3390/nano10071360.

[23] S.E. Pratsinis, Simultaneous nucleation, condensation, and coagulation in aerosol reactors, J. Colloid Interface Sci. 124 (1988) 416–427. doi:10.1016/0021-9797(88)90180-4.

[24] I. Ohnuma, H. Enoki, O. Ikeda, R. Kainuma, H. Ohtani, B. Sundman, K. Ishida, Phase equilibria in the Fe–Co binary system, Acta Mater. 50 (2002) 379–393. doi:10.1016/S1359-6454(01)00337-8.

[25] A.N. Nesmeyanov, Vapor pressure of the chemical elements, (1963).

[26] Y. Hirayama, K. Takagi, Evaluation of compositional homogeneity of Fe-Co alloy nanoparticles prepared by thermal plasma synthesis, J. Alloys Compd. 792 (2019) 594–598. doi:10.1016/j.jallcom.2019.04.083.

[27] L. Pasquini, A. Barla, A.I. Chumakov, O. Leupold, R. Rüffer, A. Deriu, E. Bonetti, Size and oxidation effects on the vibrational properties of nanocrystalline α-Fe, Phys. Rev. B - Condens. Matter Mater. Phys. 66 (2002).

[28] L. Signorini, L. Pasquini, L. Savini, R. Carboni, F. Boscherini, E. Bonetti, A. Giglia, M. Pedio, N. Mahne, S. Nannarone, Size-dependent oxidation in iron/iron oxide core-shell nanoparticles, Phys. Rev. B - Condens. Matter Mater. Phys. 68 (2003) 195423. doi:10.1103/PhysRevB.68.195423.

[29] J.M.D. Coey, Magnetism and magnetic materials, Cambridge University Press, 2009.

[30] R.J. Joenk, Second Anisotropy Constant in Cubic Ferromagnetic Crystals, Phys. Rev. 130 (1963) 932.

[31] R.S. Sundar, S.C. Deevi, Soft magnetic FeCo alloys: Alloy development, processing, and properties, Int. Mater. Rev. 50 (2005) 157–192. doi:10.1179/174328005X14339.

[32] F. Sánchez-De Jesús, A.M. Bolarín-Miró, C.A. Cortés Escobedo, G. Torres-Villaseñor, P. Vera-Serna, Structural Analysis and Magnetic Properties of FeCo Alloys Obtained by Mechanical Alloying, J. Metall. 2016 (2016) 1–8. doi:10.1155/2016/8347063.

[33] J.C. Slater, The Ferromagnetism of Nickel. II. Temperature Effects, Phys. Rev. 49 (1936) 931.

[34] W. Wernsdorfer, C. Thirion, N. Demoncy, H. Pascard, D. Mailly, Magnetisation reversal by uniform rotation (Stoner-Wohlfarth model) in FCC cobalt nanoparticles, J. Magn. Magn. Mater. 242 (2002) 132–138. doi:10.1016/S0304-8853(01)01153-2.

[35] T. Suzuki, D. Weller, C. -A. Chang, R. Savoy, T. Huang, B.A. Gurney, V. Speriosu, Magnetic and magneto-optic properties of thick face-centered-cubic Co single-crystal films, Appl. Phys. Lett. 64 (1994) 2736.

[36] P. Karipoth, A. Thirumurugan, S. Velaga, J.M. Greneche, R. Justin Joseyphus, Magnetic properties of FeCo alloy nanoparticles synthesized through instant chemical reduction, J. Appl. Phys. 120 (2016) 123906. doi:10.1063/1.4962637.

[37] G.S. Chaubey, C. Barcena, N. Poudyal, C. Rong, J. Gao, S. Sun, J.P. Liu, Synthesis and stabilization of FeCo nanoparticles, J. Am. Chem. Soc. 129 (2007) 7214–7215. doi:10.1021/ja0708969.

[38] J. Hou, Y. Kuang, H. Shen, H. Cao, L. Luo, J. Liu, P. Wan, B. Chen, X. Sun, T. Tan, Solvothermal synthesis of FeCo nanoparticles for magneto-controllable biocatalysis, RSC Adv. 4 (2014) 11136–11141. doi:10.1039/c4ra00417e.

[39] Moditma, S. Choudhary, G. Vashisht, V.R. Reddy, S. Annapoorni, Facile Synthesis of Highly Magnetic Long-term Stable FeCo Nanoparticles, J. Supercond. Nov. Magn. 33 (2020) 1653–1657. doi:10.1007/s10948-019-05398-w.

[40] W. Sucksmith, J.E. Thompson, P.R.S.L. A, The magnetic anisotropy of cobalt, Proc. R. Soc. London. Ser. A. Math. Phys. Sci. 225 (1954) 362–375. doi:10.1098/rspa.1954.0209.

[41] J. A. Osborn, Demagnetizing factors of the general Ellipsoid, Phys. Rev. 67 (1945) 351.

[42] N.A. Usov, M.S. Nesmeyanov, Multi-domain structures in spheroidal Co nanoparticles, Sci. Rep. 10 (2020) 10173. doi:10.1038/s41598-020-67173-5.